Materials Advances

ROYAL SOCIETY OF CHEMISTRY

PAPER

View Article Online
View Journal | View Issue



Cite this: *Mater. Adv.*, 2026, 7, 2454

# Synergistic effects of Sb doping and nanostructuring on spark plasma-sintered ZrNiSn thermoelectrics

José Luis Garrido-Álvarez,[a] Javier López-García,[ab] Oscar Juan Dura,[c] Matthias Schrade,[d] Anthoula Poulia,[e] Carlos F. Gutiérrez-González,[f] Marta Suárez,[g] Jesús Ángel Blanco,[a] João Elias Rodrigues,[h] Alaa Adawy,[ai] Victor Vega,[i] Ole Martin Løvvik,[de] Anette Eleonora Gunnæs[e] and Cristina Echevarria-Bonet *[a]

Nanostructured ZrNiSn and $ZrNiSn_{1-x}Sb_x$ ($x$ = 0.02 and 0.05) half-Heusler alloys were successfully synthesized *via* mechanical milling followed by spark plasma sintering. All samples crystallized in the expected MgAgAs-type crystal structure (space group $F\bar{4}3m$) and retained their nanostructured powder morphology post-sintering. Thermoelectric measurements revealed that the mechanical milling effectively reduced lattice thermal conductivity, while Sb doping significantly enhances the electrical conductivity in the ZrNiSn system. However, extending the milling time beyond 5 hours led to reduced performance due to the increased structural disorder without further thermal conductivity decrease. Hall-effect measurements yielded a relatively low effective carrier mass of around 0.7–1.3$m_e$, which accounts for the observed reduction in the Seebeck coefficient. The optimal Sb doping level was found to be $x$ = 0.02. At this doping level, a substantial improvement in thermoelectric performance is detected with a maximum thermoelectric figure of merit ($ZT$) of approximately 0.6 at 600 K (two fold that of the undoped sample) and a 60% improvement over the unmilled $ZrNiSn_{0.98}Sb_{0.02}$ alloy. These results highlight the synergistic effects of controlled Sb doping and nanostructuring *via* mechanical milling on optimizing the thermoelectric properties of ZrNiSn-based half-Heuslers.

Received 24th September 2025,
Accepted 5th December 2025

DOI: 10.1039/d5ma01100k

rsc.li/materials-advances



## Introduction

A significant amount of energy consumption in industrial processes is lost as waste heat, representing an untapped resource for energy recovery.[1] Thermoelectric (TE) materials offer a promising route for directly converting this waste heat into electricity, rendering the respective industrial processes more energy efficient.[2,3] However, the widespread application of thermoelectric devices remains limited by their relatively low conversion efficiencies.[4] The performance of a thermoelectric material is characterized by the dimensionless figure of merit, $ZT$, originally proposed by Ioffe[5] and defined as $ZT = (S^2\sigma/\kappa)T$, with $S$ referring to the Seebeck coefficient, $\sigma$ the electrical conductivity, $\kappa$ the thermal conductivity and $T$ the absolute working temperature.

To enhance their $ZT$, materials must ideally exhibit a high power factor ($S^2\sigma$) and low thermal conductivity. However, $\kappa$ includes contributions from both the lattice ($\kappa_L$) and the electronic ($\kappa_{el}$) components, the latter being expressed as $\kappa_{el} = L\sigma T$, where $L$ is the Lorenz number.[6] This coupling between $\sigma$ and $\kappa_{el}$ complicates the efforts exerted to independently optimize the thermoelectric parameters, rendering the $ZT$ enhancement attempts far from trivial. Since $S$, $\sigma$ and $\kappa_{el}$ are interdependent parameters, reducing $\kappa_L$ has been pointed out as the most effective route for improving $ZT$.[7] Several approaches have been explored to accomplish this aim, including nanostructuring, chemical substitution and the "phonon-glass electron-crystal" design strategy.[8–11]

[a] Department of Physics, University of Oviedo, Calvo Sotelo s/n, 33007 Oviedo, Spain. E-mail: echevarriacristina@uniovi.es
[b] IUTA, University of Oviedo, 33203 Gijón, Spain
[c] Department of Physics and IRICA, University of Castilla-La Mancha, Ciudad Real E-13071, Spain
[d] Department of Sustainable Energy Technology, SINTEF, Forskningsveien 1, Oslo, 0373, Norway
[e] Department of Physics, Centre for Materials Science and Nanotechnology, University of Oslo, 0316 Oslo, Norway
[f] Nanoker Research S.L., Olloniego Industrial Park, Oviedo, Spain
[g] Nanomaterials and Nanotechnology Research Center (CINN-CSIC) – University of Oviedo (UO), Principado de Asturias (PA), Avda. de la Vega, 4–6, 33940 El Entrego, Spain
[h] CELLS-ALBA Synchrotron Light Source, Cerdanyola del Vallès, Barcelona 08290, Spain
[i] Scientific and Technological Resources (SCTs), University of Oviedo, 33006 Oviedo, Asturias, Spain

Among these approaches, nanostructuring has been proven to be particularly effective by introducing grain boundaries and interfaces at the nanoscale that enhance phonon scattering and thereby reducing $\kappa_L$, without significantly affecting the electrical conductivity.[11] Additionally, nanostructuring can contribute to energy filtering and density-of-states modifications that, in turn, could enhance the Seebeck coefficient.[12] Therefore, nanostructuring can result in improving the *ZT* values and, consequently, the energy conversion efficiency.

Given this context, the thermoelectric performance of a material is strongly influenced by both its nanostructure and the employed synthesis methods. For practical applications, thermoelectric materials must meet several criteria: high and stable performance, scalability, cost-effectiveness, machinability, and thermal and chemical stability.[13] In this respect, spark plasma sintering (SPS) has emerged as a widely used method for the densification of TE materials. SPS facilitates rapid heating and electric current-assisted compaction, enabling effective consolidation while preserving the original nanostructure of the starting powdered material.[14] SPS can also be used as an alternative route to produce compounds with hierarchical microstructures from mechanically alloyed powders through reactive sintering.[15] These features make SPS particularly interesting for developing advanced thermoelectric materials with improved performance.

Semiconductors are the most promising class of thermoelectric materials owing to their electronic band structure, which permits effective coupling between thermal and electrical transport.[16] A variety of materials have been studied for TE applications, including the classical systems $Bi_2Te_3$, PbTe and $Si_{1-x}Ge_x$.[17] Among the various thermoelectric families, half-Heusler (HH) alloys have attracted considerable attention due to their excellent thermal stability, mechanical robustness at elevated temperatures, and their moderate *ZT* values at high temperatures ($\geq$600 °C).[18] These materials typically exhibit high electrical conductivity and power factors, PF = $S^2\sigma$, over a broad temperature range, but suffer from relatively high lattice thermal conductivity, which limits their overall efficiency.[19]

Half-Heusler compounds adopt the general formula XYZ, where X is an electropositive element (commonly Ti, Zr or Hf), Y is a transition metal (*e.g.* Co or Ni) and Z is a main group element (*e.g.* Sn or Sb).[20] They crystallize in a cubic MgAgAs-type crystal structure (space group $F\bar{4}3m$) in which X, Y and Z atoms occupy the Wyckoff positions 4b (1/2, 1/2, 1/2), 4c (1/4, 1/4, 1/4) and 4a (0, 0, 0), respectively.[21] Among these HH alloys, ZrNiSn-based compounds have been the subject of many related studies.[22–27] They exhibit a narrow band gap ($\sim$0.4 eV) and have demonstrated promising thermoelectric performance, with reported $ZT \approx 1$ near 1000 K through appropriate substitutions (*e.g.* Zr by Hf/Nb and Sn by Sb[28–31]). Nonetheless, their *ZT* values remain constrained by their relatively high lattice thermal conductivity. As a reference, pristine ZrNiSn usually displays lattice thermal conductivities on the order of 5–10 W m$^{-1}$ K$^{-1}$. Such elevated values reflect the inherently symmetric crystal framework and robust interatomic interactions, both of which suppress phonon-disrupting defects and maintain relatively rigid lattice dynamics.[32,33] Doping strategies—particularly those involving substitution at the X, Y, or Z sites—have been proven effective in modifying the band structure and introducing phonon-scattering centres and thereby reducing $\kappa_L$. Notable progress has been achieved by substituting Zr with Ti or Hf and Sn with Sb, as well as through reverse substitutions.

In this study, we have investigated the simultaneous enhancement of thermoelectric properties in ZrNiSn-based half-Heusler alloys through two complementary strategies: the reduction of lattice thermal conductivity *via* nanostructuring and the improvement of the power factor through Sb doping at Sn sites. To elucidate structural, microstructural, and transport–property relationships, we employed a comprehensive set of characterization techniques, including synchrotron X-ray diffraction (XRD) for phase and structural analysis, high-resolution transmission electron microscopy (HRTEM) to assess nanoscale features and disorder, and a suite of thermoelectric property measurements. These included the Seebeck coefficient, electrical conductivity, and thermal conductivity measurements to evaluate the power factor and overall figure of merit (*ZT*), as well as Hall-effect measurements to determine carrier concentration and mobility. By combining these advanced methods, we provide a detailed account on the interplay between the composition, microstructure, and transport properties, and demonstrate the effectiveness of our approach in optimizing the thermoelectric performance of ZrNiSn-based alloys.

## Experimental

Stoichiometric amounts of high-purity elemental Zr (99.8%), Ni (99.98%), Sn (99.999%) and Sb (99.999%), all supplied by Sigma-Aldrich, were used as starting materials to synthesize ZrNiSn, $ZrNiSn_{0.98}Sb_{0.02}$ and $ZrNiSn_{0.95}Sb_{0.05}$ ingots. The synthesis was performed by arc-melting under an inert argon atmosphere in a MAM-1 arc furnace (Edmund Bühler GmbH). The resulting ingots were manually ground into powders using an agate mortar and sieved through a 53 μm-mesh. The powders ($m \approx 5$ g) were subsequently subjected to mechanical milling using a Retsch PM 200 planetary ball mill an under argon atmosphere. Milling was carried out in alternating 5-minute intervals of clockwise and counterclockwise rotation, with intermediate 5-minute pauses to prevent overheating. Milling durations were 5 h for all compositions, and additionally, 10 h and 20 h for ZrNiSn. A rotation speed of 200 rpm and a ball-to-powder mass ratio of 10 : 1 were used, employing stainless steel vials (125 mL) and balls (10 mm diameter).

Densification was performed *via* SPS using a HP D 25/1 system (FCT Systeme GmbH). The milled powders were loaded into a 20 mm graphite die, separated by graphite paper, and cold-pressed. The SPS cycle involved heating to 900 °C at a rate of 100 °C min$^{-1}$ under vacuum. A uniaxial pressure of 40 MPa was initially applied at room temperature, increased to 80 MPa as the temperature reached 700 °C, and maintained at this level during the final 5-minute hold at 900 °C. Following sintering, the current and pressure were switched off, and the samples were allowed to cool spontaneously to ambient temperature.

Graphite residues were removed by polishing the pellet surfaces. The density of the sintered samples was measured using the Archimedes method, yielding values exceeding 98% of the theoretical density for all samples.

Phase purity and structural characterization were carried out using synchrotron X-ray diffraction (XRD) at beamline BL04-MSPD of the ALBA synchrotron facility, employing a wavelength of $\lambda$ = 0.4428 Å. Data were collected in the 300–600 K range. Le Bail and Rietveld refinements were performed using the FullProf Suite software package.[34] Microstructural and compositional analyses were performed using a JEOL JSM-6610LV scanning electron microscope (SEM) equipped with an energy-dispersive X-ray spectroscopy (EDS) system. High-resolution transmission electron microscopy (HRTEM) was carried out on a JEOL JEM-2100 microscope to investigate the nanoscale structural features and local disorder. Image analysis was conducted using the ImageJ software package.[35]

Thermal conductivity ($\kappa$) was determined using a Netzsch LFA 457 MicroFlash laser flash analyzer. Thermal diffusivity ($\alpha$) was measured under a nitrogen atmosphere in the temperature range of 148 to 1373 K. The thermal conductivity was calculated using the relationship $\kappa = C_P\alpha\rho$, where $C_P$ is the heat capacity and $\rho$ is the density. The density was determined using the Archimedes method, and $C_P$ was estimated using the Dulong–Petit approximation ($C_P \simeq 3R$, where $R$ is the gas constant) in the selected temperature range.[36]

Electrical resistivity was measured using the Van Der Pauw method, a four-probe technique in which a constant current is applied between two peripheral contacts, and the voltage is measured between the remaining two.[37] Hall-effect measurements to derive the carrier concentration and mobility were done with the corresponding setup configuration with field and current reversal to eliminate unwanted signals. A custom-built automated setup equipped with a Keithley 2400 source-meter was used for the measurements. The Seebeck coefficient was obtained in regular bars by comparison with a reference constantan wire utilizing the SB-100 and K-20 systems from MMR Technologies. Both electrical characterization and Seebeck coefficient measurements were performed under vacuum ($10^{-3}$ mbar) in the temperature range of 300–640 K.

## Results and discussion

Fig. 1 shows the Rietveld refinements of the XRD patterns for all ZrNiSn-based samples. The refined unit cell parameters,

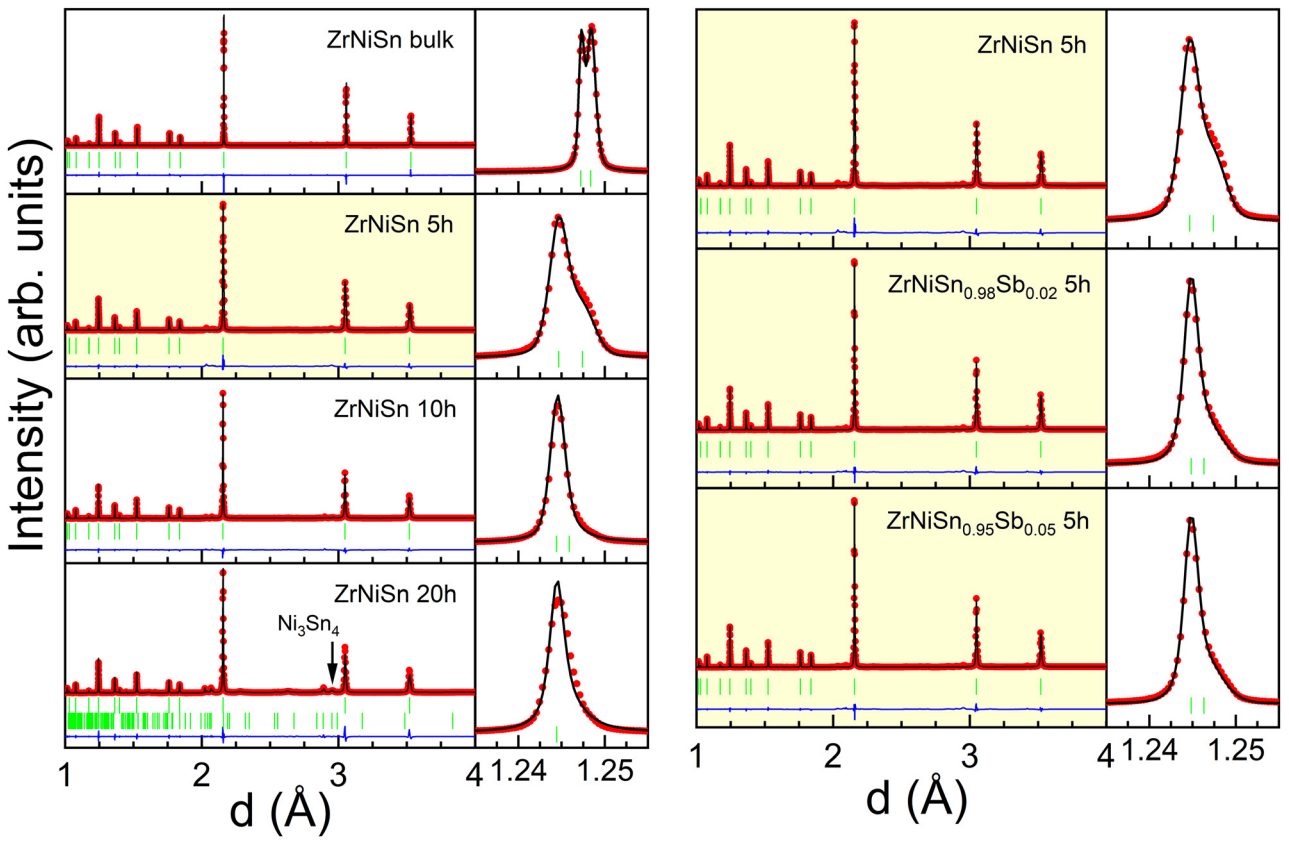


Fig. 1 Room-temperature powder XRD patterns of (left) 5, 10 and 20 h-milled ZrNiSn and (right) 5 h-milled $ZrNiSn_{1-x}Sb_x$ ($x$ = 0, 0.02 and 0.05) samples. For clarification, all 5 h-milled alloys have a yellow background. The red dots and black lines represent the experimental and calculated patterns, respectively. The blue line is the difference between the experimental and calculated patterns, while the green bars denote the Bragg positions for the cubic MgAgAs-type crystal structure. An expansion of the d-axis between 1.23 and 1.25 Å at the right of every pattern shows the Bragg peak corresponding to the (422) reflection.

Table 1 Crystal structure data for all the ball-milled ZrNiSn-based samples. $a$ and $a'$ refer to the lattice parameters of the two HH phases found in every sample

| | $x$ = 0 | $x$ = 0 | $x$ = 0 | $x$ = 0 | $x$ = 0.02 | $x$ = 0.05 |
|---|---|---|---|---|---|---|
| | Bulk | 5 h | 10 h | 20 h | 5 h | 5 h |
| Phase HH1 – $a$ (Å) | 6.1102 (1) | 6.0970 (1) | 6.0986 (1) | 6.0989 (1) | 6.0996 (1) | 6.0983 (1) |
| Abundance (wt%) | 33.86 (18) | 73.2 (9) | 79.5 (1.1) | 78.4 (4) | 75.0 (7) | 79.6 (7) |
| $R_B$ (%) | 19.7 | 3.22 | 5.23 | 4.35 | 2.75 | 3.47 |
| Phase HH2 – $a'$ (Å) | 6.1157 (1) | 6.1104 (1) | 6.1058 (1) | 6.1148 (1) | 6.1069 (1) | 6.1106 (1) |
| Abundance (wt%) | 65.6 (2) | 21.6 (5) | 14.1 (6) | 4.24 (2) | 21.7 (4) | 17.4 (4) |
| $R_B$ (%) | 25.5 | 9.05 | 9.09 | 13.8 | 5.36 | 8.28 |
| Secondary phases (%) | Sn | $Ni_3Sn_4$ | $Ni_3Sn_4$ | $Ni_3Sn_4$ | $Ni_3Sn_4$ | $Ni_3Sn_4$ |
| | 0.56 (2) | 5.22 (11) | 2.61 (10) | 9.6 (5) | 3.25 (9) | 3.02 (9) |
| | | | $NiZr_2$ | $Ni_{2.7}Sn_2$ | | |
| | | | 2.45 (16) | 6.5 (2) | | |
| | | | $Ni_{2.7}Sn_2$ | $Ni_{0.92}Sn_{0.08}$ | | |
| | | | 1.31 (10) | 0.95 (10) | | |
| | | | | $NiZr_2$ | | |
| | | | | 0.38 (7) | | |

cell volume, phase percentages and the reliability factors are listed in Table 1. All sintered samples crystallized in the expected MgAgAs-type face-centred cubic (fcc) structure (space group $F\bar{4}3m$), exhibiting a slight contraction in the cell volume (~0.3%) relative to the bulk alloy.[38]

The milled samples displayed splitting of the Bragg reflections, as seen in Fig. 1(right), indicative of phase segregation. This splitting is consistent throughout all reflections and suggests lattice duplication, consistent with previous studies.[38,39] These two phases correspond to a HH crystal structure with slight differences in the composition and lattice parameters. The broadening of the diffraction peaks, evident even at short milling times, reflects nanocrystalline domain formation, with particle sizes around 100 nm, as estimated by the Williamson–Hall analysis. These findings coincide with SEM images in Fig. 2(a) and (b).

The SEM analysis reveals that mechanical milling produces a substantial microstructural refinement, reducing the grain size from 10–15 μm in the bulk material to approximately 200–500 nm after milling, while simultaneously increasing the density of defects, irregular grain boundaries, and nanoparticle agglomerates. Such features are well known to introduce a wide spectrum of phonon-scattering centres. In particular, the high density of grain boundaries in the nanostructured material increases phonon boundary scattering, which is especially effective for mid- to long-wavelength phonons that typically dominate heat transport in half-Heusler alloys. Additionally, strain fields, dislocations, and interface mismatches associated with the mechanically induced defects further disrupt phonon propagation by enhancing point-defect and strain-field scattering. The average crystallite size estimated by the Williamson–Hall method (~100 nm) is smaller than the apparent particle size observed by SEM, suggesting that each SEM-visible particle consists of several nanocrystalline domains. The SI provides complementary SEM evidence that strengthens our microstructural analysis. Fig. S1 documents the evolution of the microstructure throughout the full synthesis route for all milling durations, from the bulk precursor to the milled powders and finally to the SPS-consolidated pellets. This sequence highlights the progressive grain refinement and defect generation induced by mechanical milling, as well as the extent to which these features are preserved or recovered during SPS. In addition, Fig. S2 displays SEM micrographs of the ball-milled powders at multiple magnifications, offering a detailed view of the particle-size reduction, agglomeration behaviour, and surface morphology resulting from milling.

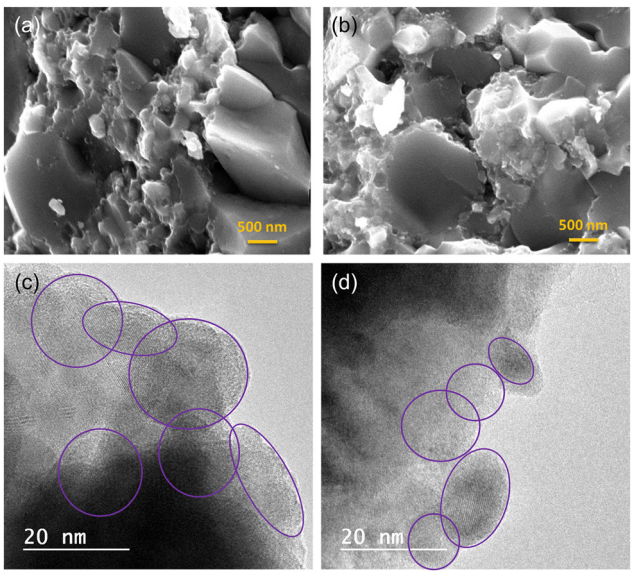


Fig. 2 (a) and (b) Scanning electron microscopy and (c) and (d) high-resolution transmission electron microscopy images of the (a) and (c) $ZrNiSn_{0.98}Sb_{0.02}$ and (b) and (d) $ZrNiSn_{0.95}Sb_{0.05}$ samples (both milled for 5 hours). Micro- and submicrometric particles are clearly visible in the SEM micrographs. On the other hand, the HRTEM images confirm the presence of nanocrystalline domains (confirmed by the visible lattice fringes) and indicated by circles.

Since XRD is not suitable for accurately quantifying Sb content, elemental compositions were determined *via* SEM-EDS. The obtained normalized stoichiometries, $Zr_{1.08(10)}Ni_{0.87(8)}Sn_{1.00(3)}Sb_{0.05(1)}$ and $Zr_{0.99(10)}Ni_{0.92(9)}Sn_{1.00(2)}Sb_{0.09(1)}$ for $x$ = 0.02 and $x$ = 0.05 alloys, respectively, are broadly consistent with the nominal compositions, though a slight excess of Sb is noted.

Nevertheless, for simplicity, the samples are referred to using their nominal compositions throughout the text. In addition to particles ~100 nm in size, HRTEM images [Fig. 2(c) and (d)] reveal the presence of aggregated nanoparticles within the grains in the 10–20 nm range.

Except for the bulk (ZrNiSn 0 h) sample, all the milled samples exhibit a primary HH phase with a reduced lattice parameter $a$, representing approximately 75 wt% of the total phase content, and a secondary HH phase with a larger lattice parameter $a'$, whose abundance varies between 4 and 22 wt%, depending on the presence of secondary phases. In the bulk sample, the HH phase with the larger lattice parameter is the dominant one, accounting for 66 wt% of the total, and the only detected secondary phase is elemental Sn, with an abundance below 1 wt%. In contrast, the sample milled for 20 hours contains a significant number of secondary phases, rounding to nearly 20 wt% of the sample, including $Ni_3Sn_4$, $Ni_{2.7}Sn_2$, $Ni_{0.92}Sn_{0.08}$, and $NiZr_2$. For the other milled samples, $Ni_3Sn_4$ is the predominant secondary phase, with abundances ranging from 2 to 5 wt%. In the 10 h-milled sample, minor amounts (<3 wt%) of $NiZr_2$ and $Ni_{2.7}Sn_2$ were also identified. These results suggest that extended milling duration resulted in the formation of secondary phases, which may adversely affect the thermoelectric properties of the material. HRTEM images in Fig. 3 confirm the coexistence of ZrNiSn nanocrystals and $Ni_3Sn_4$ precipitates (highlighted with purple circles), along with evident structural disorder at the grain boundaries in the ZrNiSn sample milled for 20 hours. These observations demonstrate that the SPS process effectively preserves the nanostructure of the starting powder.

The linear coefficient of thermal expansion, (CTE, $\alpha$), was determined for the milled samples from the Rietveld-refined lattice parameters using the relationship $\alpha = \frac{1}{a}\left(\frac{\Delta a}{\Delta T}\right)$. The calculated CTE values are listed in Table 2. A linear dependence of the lattice parameters with temperature was observed across the range 300–900 K (not shown), validating the assumption of constant $\alpha$. For example, $\alpha_{ZrNiSn}$ values between = 0.893 × $10^{-5}$ $K^{-1}$ and 0.958 × $10^{-5}$ $K^{-1}$ agree well with theoretical estimates from a quasiharmonic approximation within density functional theory (DFT) using the supercell finite displacement method (FDM)[40] and experimental values reported elsewhere.[39,41] Compared to other thermoelectric materials, such as skutterudites, clathrates, or $Bi_2Te_3$, the CTE of ZrNiSn lies in an intermediate range.

Table 2 Linear CTE for the $ZrNiSn_{1-x}Sb_x$ HH alloys. The Debye temperatures, $\theta_D$, and the anharmonicity factor, $A$, are obtained from fittings of temperature-dependent ADPs (Fig. 4) to eqn (1)

| Material | CTE ($10^{-5}$ $K^{-1}$) | $D$ (K) | $A$ ($10^{-6}$ $K^{-1}$) |
|---|---|---|---|
| ZrNiSn 5 h | 0.958 (3) | 216 (7) | 2.56 (8) |
| ZrNiSn 10 h | 0.893 (1) | 202 (4) | 1.66 (7) |
| ZrNiSn 20 h | 0.903 (1) | 217 (5) | 2.55 (13) |
| $ZrNiSn_{0.98}Sb_{0.02}$ 5 h | 0.851 (5) | 197 (7) | 2.25 (5) |
| $ZrNiSn_{0.95}Sb_{0.05}$ 5 h | 0.861 (4) | 185 (5) | 2.21 (4) |

The Sb-doped ZrNiSn samples milled for 5 hours exhibit a noticeably reduced CTE when compared to the undoped compound. At the atomic scale, this behaviour can be attributed to reduced bond anharmonicity, as the CTE is closely linked to the anharmonic component of the interatomic potential.[42] Moreover, the CTE tends to saturate at high temperatures, akin to the temperature-dependent specific heat ($\alpha \propto C_V(T)$). Since the Debye temperature ($\theta_D$) governs both thermal expansion and specific heat, its evaluation provides further insight into the lattice dynamics.

Atomic displacement parameters (ADPs), obtained from Rietveld refinement as $B_{iso}$ values, provide additional information about structural disorder and vibrational properties. For cubic structures, the isotropic displacement $\langle U_{iso}{}^2 \rangle$ is assumed so that $B_{iso} = 8\pi^2 \langle U_{iso}{}^2 \rangle$. These values were averaged over atomic sites to determine the global mean displacement for each phase, as plotted in Fig. 4(left). The Debye model was used to analyse the temperature dependence of $\langle U_{iso}{}^2 \rangle$:

$$\langle U_{iso}{}^2 \rangle = \frac{3\hbar^2 T}{m k_B \theta_D{}^2}\left[\frac{T}{\theta_D}\int_0^{\frac{\theta_D}{T}} \frac{x}{e^x - 1}dx + \frac{\theta_D}{4T}\right] \quad (1)$$

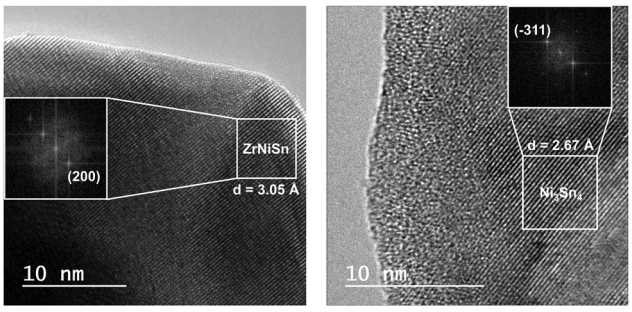


Fig. 3 High-resolution transmission electron microscopy images of the 20 h-milled ZrNiSn sample. The insets show the crystallographically analyzed fast Fourier transforms of the ZrNiSn and $Ni_3Sn_4$ crystalline phases.

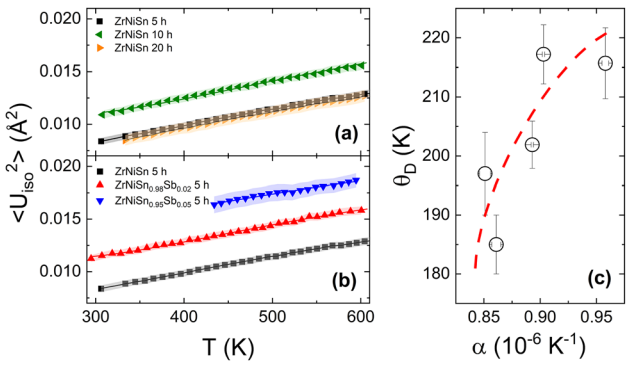


Fig. 4 Temperature-dependent isotropic ADPs ($\langle U_{iso}{}^2 \rangle$) for the experimental data (dots) and calculated values $\langle U_{iso}{}^2 \rangle$ (continuous line), for the (a) mechanically milled ZrNiSn and the (b) 5 h-milled ZrNi(Sn,Sb) alloys. (c) The relationship between the Debye temperature and the coefficient of thermal expansion in mechanically milled ZrNi(Sn,Sb). The dashed line is a guide for the eye.

where $\hbar$ is the reduced Planck constant, $k_B$ is the Boltzmann constant, $m$ is the average mass, $\theta_D$ is the Debye temperature and $T$ is the absolute temperature. The Debye temperature is typically temperature-dependent and can be determined using the Thirring-Stern expansions derived from the quasiharmonic formulation of thermodynamic functions, such as the thermal energy $W_{th}^{h}$.[43] Therefore, the quasiharmonic Debye temperature for the thermal energy can be expressed as $\theta_W^h = \theta_1 + \sum_{n=1}^{\infty} b_n T^{-n}$, with $b_n$ being fitting coefficients of the Thirring–Stern expansions[43] and $\theta_1$ representing a characteristic temperature linked to the vibrational modes of the crystal lattice. When these characteristic temperatures converge to the Debye temperature, the formulation simplifies to the classical Debye model. Nevertheless, to more accurately describe the system's behavior, it is essential to incorporate not only the quasiharmonic approximation but also anharmonic effects. As a result, the Debye temperature becomes temperature-dependent and can be determined through the following expression:

$$\theta_W = \theta_W^h + \frac{\frac{1}{2}AT^2}{\frac{d\left(\frac{W_{th}^h}{3Nk_BT}\right)}{d\left(\frac{\theta_W^h}{T}\right)}} \quad (2)$$

The coefficient $A$ reflects the degree of anharmonicity in the system and must satisfy the condition $|AT| < 1$ to ensure that the model remains applicable. The ADPs were fitted using eqn (1), incorporating the temperature-dependent Debye temperature, $\theta_D$, as derived from eqn (2). These fits are illustrated in Fig. 4. The resulting Debye temperatures ($\theta_1$, hereafter denoted as $\theta_D$) and the corresponding anharmonicity coefficients $A$ obtained from the fitting procedure are summarized in Table 2. Values of $A$ are notably low, indicating minimal anharmonic contributions, in agreement with previously reported studies.[39,41–44]

Fig. 5 displays the temperature dependence of the total and lattice thermal conductivity ($\kappa$ and $\kappa_L$, respectively) of the undoped and Sb-doped ZrNiSn milled alloys. $\kappa_L$ was estimated by subtracting the electronic contribution from the total thermal conductivity (Fig. 5(a) and (b)), using the Wiedemann–Franz law with a Lorenz number $L = 2 \times 10^{-8}$ W Ω K$^{-2}$, appropriate for ZrNiSn.[45] At high temperatures ($T > \theta_D$), $\kappa_L$ typically follows a power-law dependence, $\kappa_L(T) \propto T^{-x}$. For undoped ZrNiSn, low values of $x$ indicate weak temperature dependence (see Fig. 5(c)). Moreover, a reduction of $x$ from 0.45 to 0.05 indicates a transition from an Umklapp phonon–phonon scattering dominated regime to a disorder/boundary scattering regime, consistent with phonon-glass-like behavior.[46] The combined effect of the microstructural features (see above) results in a marked suppression of $\kappa_L$, consistent with the observed reduction in thermal conductivity for the 5-h milled sample. Thus, the enhanced phonon scattering introduced by the

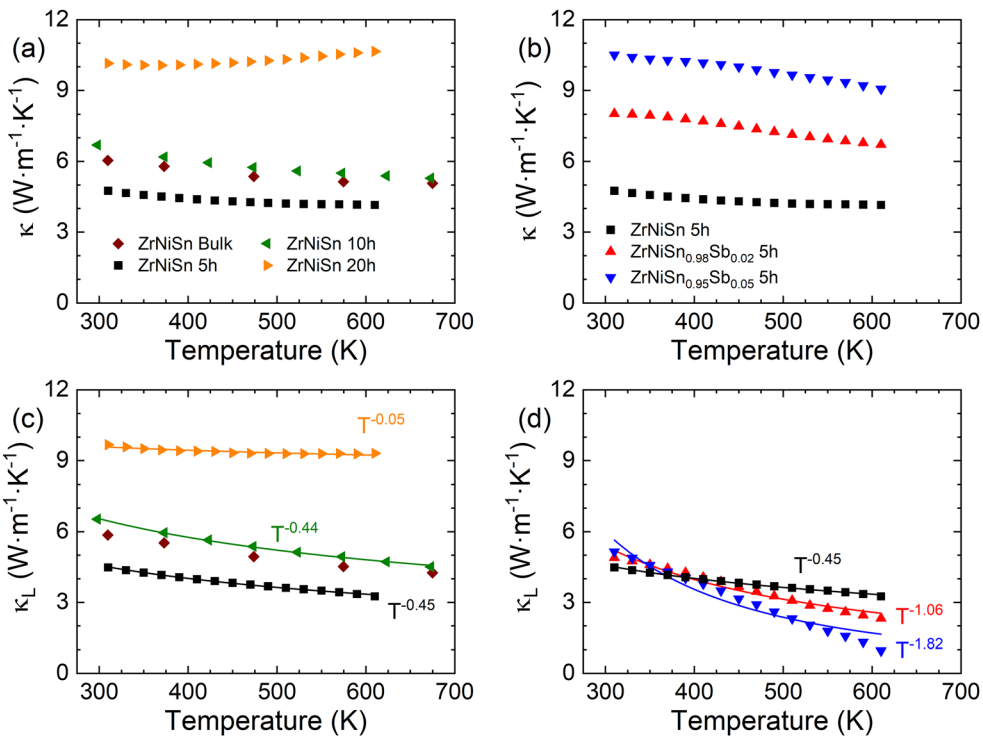


Fig. 5 Temperature dependence of the (a) and (b) thermal conductivity and (c) and (d) lattice thermal conductivity, for (a) and (c) 5-, 10- and 20-h milled ZrNiSn ($x$ = 0) and (b) and (d) 5-h milled $ZrNiSn_{1-x}Sb_x$ samples, compared to bulk data, from the literature.[22] Solid lines correspond to a power-law dependence, typical behavior of the $\kappa_L(T)$ at high temperatures.

refined and defect-rich microstructure provides a coherent explanation for the decrease in lattice thermal conductivity.

The dependence of the lattice thermal conductivity on milling time reflects a balance between microstructural refinement and the progressive formation of secondary phases. After 5 h of mechanical milling, the marked grain-size reduction and increased defect density (irregular grain boundaries, dislocations, and nanoparticle agglomerates) maximize phonon scattering at the interfaces and defect sites, leading to the lowest $\kappa_L$ observed in this series. At this stage, the content of secondary phases remains relatively limited, so heat transport is still dominated by the nanostructured $ZrNiSn_{1-x}Sb_x$ matrix. For longer milling times (10 and 20 h), however, the fraction of secondary phases (Sn, $Ni_3Sn_4$, $NiZr_2$, $Ni_{2.7}Sn_2$, and $Ni_{0.92}Sn_{0.08}$) increases significantly, as revealed by Rietveld refinements (Table 1). Many of these impurity phases are metallic or possess relatively high thermal conductivity, and their growing volume fraction and possible partial connectivity provide additional paths for heat transport. As a consequence, the beneficial reduction of $\kappa_L$ achieved by nanostructuring is progressively offset, and an increase in the effective lattice thermal conductivity is observed for the 10-h and 20-h milled samples, to the detriment of the overall phonon-blocking efficiency of the composite microstructure.

On the other hand, upon Sb doping (see Fig. 5(d)), the exponent $x$ increases from 0.45 to 1.82 (strong temperature dependence), which indicates a shift from defect-dominated phonon scattering to a regime dominated by intrinsic Umklapp processes (phonon–phonon scattering). The introduction of Sb point defects reduces the phonon mean free path and thereby lowering $\kappa_L$. Therefore, Sb doping not only modulates the carrier concentration (and hence the Seebeck coefficient and electrical conductivity) but also reduces lattice thermal conductivity, which may lead to an enhancement of the thermoelectric figure of merit $zT$.

The temperature dependence of the electrical conductivity is displayed in Fig. 6(a) and (b) for the undoped and Sb-doped ZrNiSn milled alloys. Pure ZrNiSn exhibits typical semiconducting behaviour, with $\sigma$ increasing with temperature. The values of $\sigma$ are comparable across all undoped samples and agree with literature reports,[22] indicating similar carrier concentrations. In contrast, Sb-doped samples exhibit degenerate semiconductor behaviour with $\sigma \propto T^{-0.5}$, also consistent with previous studies,[22] and show more metallic-like behaviour due to increased electron concentrations.

The Seebeck coefficient in Fig. 6(c) and (d) for undoped and doped samples, respectively, reveal negative values across the entire temperature range, confirming the majority of n-type charge carriers. $|S|$ increases with temperature, peaking up near 600 K. Both milling time and Sb-doping reduce the value of $|S|$, with the $x$ = 0.05 alloy showing notably low values, indicating an increased carrier concentration. Compared to bulk ZrNiSn, the Seebeck coefficient values are significantly lower, prompting Hall-effect measurements on 5-hour-milled ZrNi(Sn,Sb) samples to assess carrier mobility and density. Table 3 summarizes the thermoelectric properties of the doped and undoped samples, compared to bulk literature values.

Fig. 7(a) shows that Hall carrier density, $n_H$, can be tuned by modifying the Sb content. $n_H$ increases with temperature across all compositions, indicating the presence of impurity states or the thermal excitation of minority carriers. Fig. 7(b) demonstrates a linear increase of $n_H$ with the Sb amount, in agreement

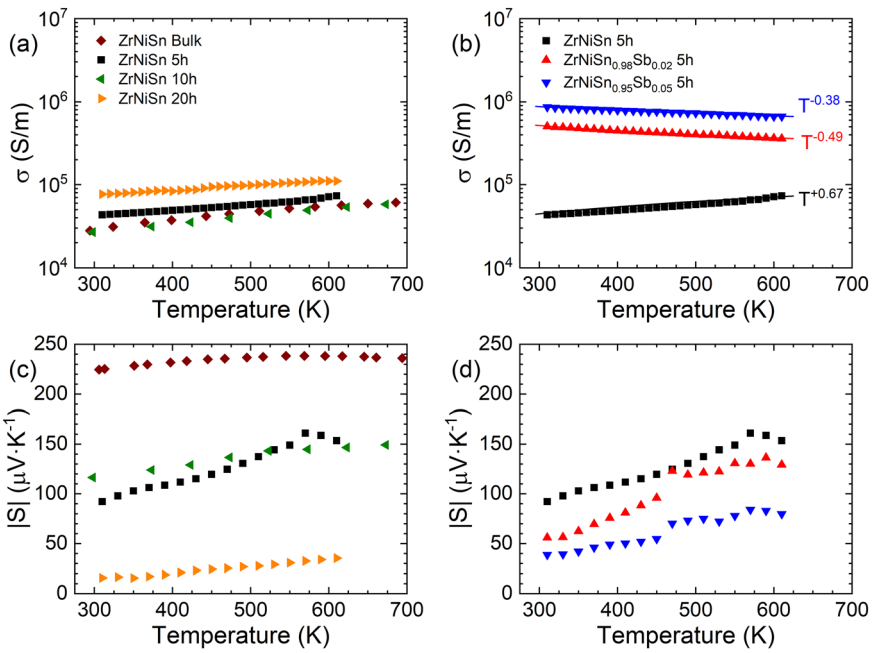


Fig. 6 Temperature dependence of the (a) and (b) electrical conductivity and (c) and (d) Seebeck coefficient, for (a) and (c) milled ZrNiSn ($x$ = 0) and (b) and (d) 5-h milled $ZrNiSn_{1-x}Sb_x$ samples, compared to bulk data, from the literature.[22] Solid lines correspond to a power-law dependence.

Table 3 Values of the magnitudes: module of the Seebeck coefficient, $|S|$; electrical conductivity, $\sigma$; total thermal conductivity, $\kappa$; lattice thermal conductivity, $\kappa_L$; and figure of merit, $ZT$ at 600 K for ZrNiSn-based samples and compared to ZrNiSn bulk values, obtained from the literature.[22]

| | ZrNiSn | ZrNiSn | ZrNiSn | ZrNiSn | $ZrNiSn_{0.98}Sb_{0.02}$ | $ZrNiSn_{0.95}Sb_{0.05}$ |
|---|---|---|---|---|---|---|
| | 0 h | 5 h | 10 h | 20 h | 5 h | 5 h |
| $\lvert S\rvert$ ($\mu V\ K^{-1}$) | 238 | 158 | 146 | 34.7 | 131 | 81.2 |
| $\sigma$ ($10^4\ S\ m^{-1}$) | 5.52 | 7.15 | 5.17 | 11.1 | 3.68 | 67.4 |
| $\kappa$ ($W\ m^{-1}\ K^{-1}$) | 5.11 | 4.16 | 5.45 | 10.6 | 6.75 | 9.14 |
| $\kappa_L$ ($W\ m^{-1}\ K^{-1}$) | 4.45 | 3.35 | 4.81 | 9.30 | 2.38 | 1.14 |
| $ZT$ | 0.36 | 0.25 | 0.12 | 0.01 | 0.57 | 0.28 |

with the simple valence model, where each Sb atom contributes one additional electron.[47] However, the measured $n_H$ values exceed expectations, likely due to intrinsic point defects or a slight excess of Sb beyond the nominal composition, as confirmed by SEM-EDS analysis.

The temperature dependence of the Hall mobility, $\mu_H$, is displayed in Fig. 7(c). For the undoped ZrNiSn sample, $\mu_H$ exhibits a $T^{-0.5}$ dependence, indicating that alloy scattering is the dominant mechanism for the charge carrier transport. In contrast, Sb-doped samples follow a $T^{-1.5}$ dependence, consistent with acoustic phonon scattering as the primary-limiting factor for carrier mobility and with previous electrical conductivity measurements (Fig. 6(b)). These observations support the conclusion that doping alters the scattering regime from impurity-dominated to phonon-limited transport. The significantly higher carrier mobility observed upon Sb incorporation can be primarily attributed to the reduction in ionized-impurity scattering enabled by optimal donor doping. In undoped, nominally "pure" ZrNiSn, the relatively high intrinsic carrier concentration originates from native point defects—such as Zr interstitials or Sn vacancies—that behave as strong ionized scatterers. These defects generate highly disruptive Coulomb potentials that efficiently scatter charge carriers and thus limit mobility. When Sb substitutes for Sn, it acts as a controlled and energetically favourable donor, increasing the electron concentration while simultaneously suppressing the formation of these native defects. As a result, the overall density of ionized scattering centres decreases, and the lattice becomes electronically more ordered, facilitating carrier transport. Beyond defect passivation, Sb doping also induces subtle band-structure modifications that further assist mobility: first-principles studies on related half-Heusler systems[48–50] show that Sb substitution can promote partial conduction-band convergence and slightly reduce the electronic effective mass. In parallel, improved densification and cleaner grain boundaries in Sb-doped samples are confirmed through SEM analysis

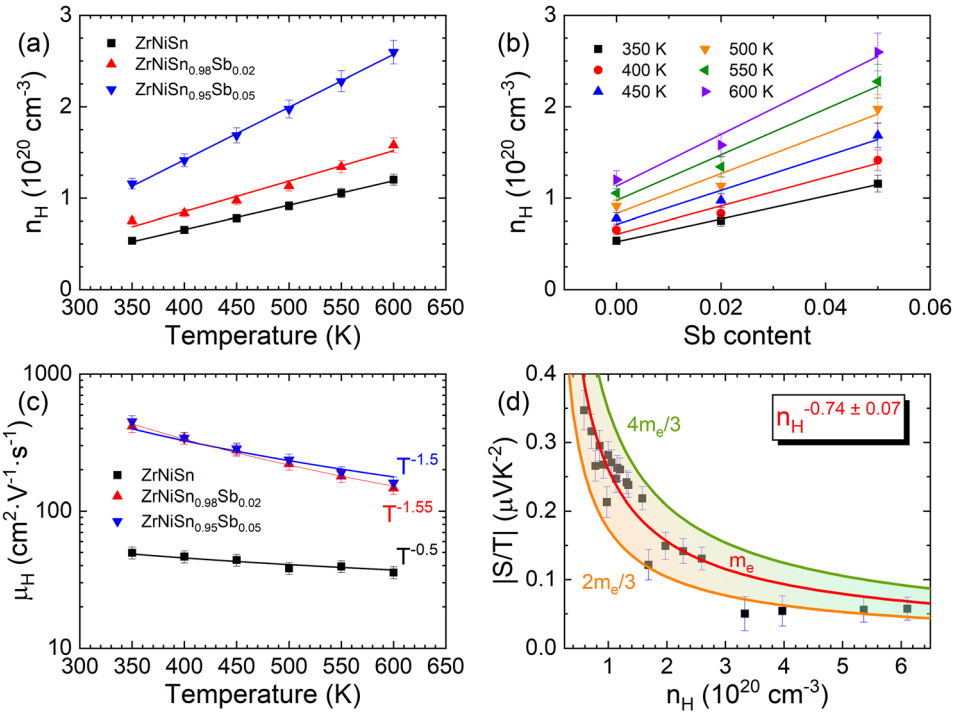


Fig. 7 Temperature dependence of (a) $n_H$ and (b) $\mu_H$. Dashed lines correspond to a linear fit. (c) $n_H$ as a function of the Sb amount. Dashed lines follow a power-law dependence. (d) Carrier density dependent $|S/T|$. Solid lines correspond to simulated curves based on the single parabolic band model (see text for more details).

(Fig. 2)—mitigate grain-boundary scattering by lowering interfacial potential barriers. Altogether, these combined mechanisms consistently explain the substantial mobility enhancement across the measured temperature range in Sb-doped ZrNiSn alloys.

To further interpret these trends and explore the interplay between electrical conductivity, Seebeck coefficient, and carrier concentration, the single parabolic band (SPB) model can be applied. This model provides a useful framework to correlate the thermoelectric transport properties with the band structure and scattering mechanisms, so that:

$$S = T\frac{8\pi^2 k_B^2 m^*}{3eh^2}\left(\frac{\pi}{3n}\right)^{2/3}$$

where $k_B$ is the Boltzmann constant, $m^*$ is the effective mass, $h$ is the Planck constant and $n$ is the charge carrier concentration.[16]

Fig. 7(d) presents the Seebeck coefficient normalized by temperature ($S/T$) as a function of the Hall carrier density $n_H$. The experimental data are compared with simulated curves based on the SPB model, showing good agreement. For this calculation, the density-of-states (DOS) effective mass $m^*$ was assumed to be temperature-independent, a simplification that is generally not accurate. However, previous studies reported that $m^*$ varies by less than 8% between 300 and 800 K for ZrNiSn,[22] rendering this approximation reasonable for the considered temperature range. The effective mass derived from the SPB fitting would be around 0.7–1.3$m_e$ (in the 350–600 K range), lower values than those typically reported for ZrNiSn-based materials. Since tuning $m^*$ is essential for optimizing the carrier concentration $n_H$, these anomalously low values may account for the relatively poor Seebeck coefficient and reduced carrier density observed in our samples.[51]

The thermoelectric figure of merit $ZT$ is depicted as a function of temperature and Hall mobility in Fig. 8(a) and (b), respectively. Consistent with previous studies on undoped ZrNiSn,[52] no significant improvement in the figure of merit is observed upon combining high-energy ball milling with subsequent SPS. This lack of enhancement is likely associated with the relatively high sintering temperature (1223 K) and prolonged dwell time (15 min) used by Xie *et al.*, which can promote extensive grain growth and defect recovery, thereby suppressing the nanostructure introduced by ball milling. A moderate improvement has been reported elsewhere[53] for samples containing excess Ni, where the introduction of controlled antisite defects leads to additional phonon scattering and a modest increase in $ZT$.

In our work, the 5-hour-milled sample achieves $ZT$ values of approximately 0.3 at 600 K, comparable to those of the bulk material, despite a significant reduction in lattice thermal conductivity. In contrast, samples milled for 10 and 20 hours exhibit reduced $ZT$ values, primarily due to a notable decrease in the Seebeck coefficient and a partial recovery of the lattice thermal conductivity. This degradation in performance is likely to be attributed to the structural disorder, including partial amorphization or the presence of secondary phases, which arose during extended mechanical milling.

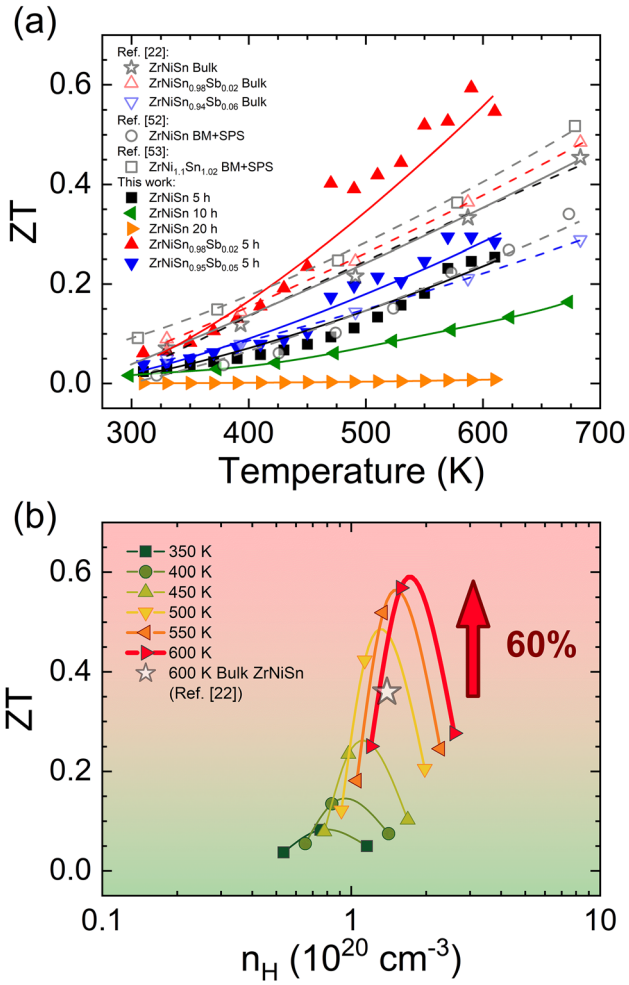


Fig. 8 Figure of merit as a function of (a) temperature and (b) carrier density for ZrNiSn-based samples and compared with representative literature data for ZrNiSn-based alloys.[22,52,53] Continuous (dashed) lines are just guides for the eye for experimental (literature) values.

For the 5-h milled $ZrNiSn_{1-x}Sb_x$ ($x$ = 0.02 and 0.05) samples, the optimal doping level was found to be $x$ = 0.0.2, achieving a maximum $ZT$ value of approximately 0.6 at 600 K. This result aligns with previous findings[22] and highlights the effectiveness of combining nanostructuring with moderate Sb doping. Specifically, the $ZT$ of the $x$ = 0.0.2 sample shows an enhancement of nearly 100% at 600 K compared to the undoped ($x$ = 0) counterpart. This improvement arises from the synergistic effects of reduced lattice thermal conductivity due to mechanical milling and enhanced electrical conductivity, resulting from the optimized carrier concentration induced by Sb doping. Overall, mechanical milling alone leads to an approximate 50% increase in $ZT$ at 600 K compared to the bulk alloy,[22] primarily by lowering the lattice thermal conductivity. Fig. 8(b) further shows that both $ZT$ and the optimal Hall carrier concentration increase with temperature up to 600 K. The optimal carrier density is found to be around $n_H \approx 2 \times 10^{20}$ cm$^{-3}$, which is slightly lower than values reported in earlier studies. This difference may reflect variations in sample

processing or the interplay between nanostructuring and doping levels.

## Conclusions

In summary, it was established that spark plasma sintering can produce compact $ZrNiSn_{1-x}Sb_x$ ($x$ = 0, 0.02 and 0.05) pellets, maintaining the original nanostructure of the starting powdered material. Mechanical milling significantly improved the thermoelectric performance of ZrNi(Sn,Sb) alloys by reducing the grain size to the nanoscale, thereby promoting enhanced carrier scattering. The main mechanism of thermal transport was phonon–phonon scattering for ZrNiSn and point-defect scattering for Sb-doped samples. However, milling durations beyond 5 h introduced grain boundary disorder and an increase of the amount of secondary phases, which worsened the thermoelectric properties of the ZrNiSn alloys. The electrical transport in the undoped ZrNiSn alloy was primarily dominated by alloy scattering, while in the doped alloys, the carrier mobility was limited by acoustic phonon scattering. These modifications have led to an optimized balance between electrical conductivity and thermal transport, thereby improving the overall figure of merit ($ZT$). The highest value of the figure of merit was achieved for the 5-hour-milled $ZrNiSn_{0.98}Sb_{0.02}$ sample ($ZT$ = 0.6 at 600 K); 100% larger than that for the 5-hour-milled undoped ZrNiSn alloy, and 50% more than that for the $ZrNiSn_{0.98}Sb_{0.02}$ bulk. These results highlight the strong synergistic effect of coupling moderate doping with nanostructuring: while Sb doping increases the carrier concentration and improves electrical conductivity, mechanical milling reduces the lattice thermal conductivity through enhanced phonon scattering at grain boundaries and defects. Together, these effects converge to optimize the thermoelectric properties, demonstrating that careful tuning of both composition and nanostructure is key to achieving high-performance half-Heusler-based thermoelectrics.

## Author contributions

J. L. Garrido Álvarez: investigation, formal analysis, and writing – original draft. J. López García: formal analysis, investigation, and writing – final review & editing. O. J. Durá: validation, formal analysis, investigation, visualization, and writing – review & editing. M. Schrade: investigation, conceptualization, and final review & editing. A. Poulia: investigation. C. F. Gutiérrez-González: investigation. M. Suárez: investigation and final review & editing. J. A. Blanco: funding acquisition, visualization, conceptualization, and writing – review & editing. J. E. Rodriguez: investigation. A. Adawy: investigation and final review & editing. V. Vega: investigation. O. M. Løvvik: supervision, conceptualization, and final review & editing. A. E. Gunnæs: supervision. C. Echevarria Bonet: funding acquisition, conceptualization, methodology, investigation, formal analysis, supervision, visualization, and writing – original draft, and final review & editing.

## Conflicts of interest

There are no conflicts to declare.

## Data availability

Data for this article, including the .CIF file and SEM and TEM images, are available at Zenodo at https://doi.org/10.5281/zenodo.17037943 and https://doi.org/10.5281/zenodo.17037905, respectively.

Supplementary information (SI) is available. See DOI: https://doi.org/10.1039/d5ma01100k.

## Acknowledgements

This work was supported by the SEKUENS Agency of the Principality of Asturias (SEK-25-GRU-GIC-24-113) and MICIU/AEI/10.13039/501100011033/and ERDF, UE (PID22-138256N3-C21). The work of C. Echevarria-Bonet was also supported by Banco Santander for their Mobility grants for lecturers and researchers from the University of Oviedo for research stays at foreign institutions (2021–22) and in external companies (2021). J. L. Garrido thanks the Principality of Asturias for supporting his PhD studies at the University of Oviedo (project number: SV-PA-21-AYUD/2021/51822) and the Gijón City Council for the research grant Cátedra Milla del Conocimiento: Gijón SMART CITIES. A. Adawy acknowledges her Ramon y Cajal grant received from the Spanish Ministry of Science and Innovation (RYC2022-038426-I). O. M. Løvvik and A. E. Gunnæs acknowledge financial support from the Research Council of Norway through the Allotherm project (No. 314778). The authors acknowledge the technical support received from Nanoker Research personnel during the development of this investigation, the skillful assistance of the staff at the BL04-MSPD beamline, at ALBA synchrotron, Barcelona, Spain and the technical support provided by Servicios Científico-Técnicos de la Universidad de Oviedo.

## References

1 G. Kosmadakis, *Appl. Therm. Eng.*, 2024, **246**, 122957.
2 Q. Sun, C. Du and G. Chen, *Prog. Mater. Sci.*, 2025, **149**, 101402.
3 P. Baskaran and M. Rajasekar, *RSC Adv.*, 2024, **14**, 21706–21744.
4 J. He, K. Li, L. Jia, Y. Zhu, H. Zhang and J. Linghu, *Appl. Therm. Eng.*, 2024, **236**, 121813.
5 A. F. Ioffe, *Semiconductor Thermoelements and Thermoelectric Cooling*, Info-search Ltd., London, 1st edn, 1957.
6 X. Zhang and L.-D. Zhao, *J. Materiomics*, 2015, **1**, 92–105.
7 H. Han, L. Zhao, X. Wu, B. Zuo, S. Bian, T. Li, X. Liu, Y. Jiang, C. Chen, J. Bi, J. Xu and L. Yu, *J. Mater. Chem. A*, 2024, **12**, 24041–24083.
8 M. F. Masoud, S. Butt, M. Waseem Akram, N. Naeem, A. Irfan, A. Abbas and S. Irfan, *RSC Adv.*, 2025, **15**, 9854–9863.

9 C. Wu, X. L. Shi, L. Wang, W. Lyu, P. Yuan, L. Cheng, Z. G. Chen and X. Yao, *ACS Nano*, 2024, **18**, 31660–31712.
10 V. Taneja, S. Das, K. Dolui, T. Ghosh, A. Bhui, U. Bhat, D. K. Kedia, K. Pal, R. Datta and K. Biswas, *Adv. Mater.*, 2024, **36**, 2307058.
11 P. Xu, K. Jin, J. Huang, Z. Yan, L. Fu and B. Xu, *Nanoscale*, 2025, **17**, 10531–10556.
12 T. G. Novak, K. Kim and S. Jeon, *Nanoscale*, 2019, **11**, 19684–19699.
13 W.-T. Chiu, C.-L. Chen and Y.-Y. Chen, *Sci. Rep.*, 2016, **6**, 23143.
14 P. Cavaliere, B. Sadeghi and A. Shabani, *Spark Plasma Sintering of Materials, Springer International Publishing*, Cham, 2019, pp. 3–20.
15 X. Ai, Y. Wu, H. Lyu, L. Giebeler, W. Xue, A. Sotnikov, Y. Wang, Q. Zhang, D. Makarov, Y. Yu, G. J. Snyder, K. Nielsch and R. He, *Nat. Commun.*, 2025, **16**(1), 6497.
16 G. J. Snyder and E. S. Toberer, *Nat. Mater.*, 2008, **7**, 105–114.
17 *Thermoelectrics handbook: macro to nano*, ed. D. M. Rowe, CRC Press, Boca Raton, 1st edn, 2006.
18 L. Huang, Q. Zhang, B. Yuan, X. Lai, X. Yan and Z. Ren, *Mater. Res. Bull.*, 2016, **76**, 107–112.
19 S. J. Poon, *Metals*, 2018, **8**, 989.
20 J.-W. G. Bos and R. A. Downie, *J. Phys.: Condens. Matter*, 2014, **26**, 433201.
21 A. Ojha, R. K. Sabat and S. Bathula, *Mater. Sci. Semicond. Process.*, 2024, **171**, 107996.
22 H. Xie, H. Wang, C. Fu, Y. Liu, G. J. Snyder, X. Zhao and T. Zhu, *Sci. Rep.*, 2014, **4**, 6888.
23 X. Yang, Z. Jiang, J. Li, H. Kang, D. Liu, F. Yang, Z. Chen, E. Guo, X. Jiang and T. Wang, *Nano Energy*, 2020, **78**, 105372.
24 K. K. Johari, R. Bhardwaj, N. S. Chauhan, S. Bathula, S. Auluck, S. R. Dhakate and B. Gahtori, *ACS Appl. Energy Mater.*, 2021, **4**, 3393–3403.
25 R. Min, Y. Wang, X. Jiang, R. Chen, H. Kang, E. Guo, Z. Chen, X. Yang and T. Wang, *Chem. Eng. J.*, 2022, **449**, 137898.
26 R. Yan, C. Shen, M. Widenmeyer, T. Luo, R. Winkler, E. Adabifiroozjaei, R. Xie, S. Yoon, E. Suard, L. Molina-Luna, H. Zhang, W. Xie and A. Weidenkaff, *Mater. Today Phys.*, 2023, **33**, 101049.
27 L. Hu, S. Han, T. Zhu, T. Deng and C. Fu, *npj Comput. Mater.*, 2025, **11**, 1–10.
28 J. Zhang, X. Zhang and Y. Wang, *Sci. Rep.*, 2017, **7**, 14590.
29 C. Yu, T.-J. Zhu, K. Xiao, J.-J. Shen, S.-H. Yang and X.-B. Zhao, *J. Electron. Mater.*, 2010, **39**, 2008–2012.
30 L. Chen, S. Gao, X. Zeng, A. Mehdizadeh Dehkordi, T. M. Tritt and S. J. Poon, *Appl. Phys. Lett.*, 2015, **107**, 041902.
31 S. Sakurada and N. Shutoh, *Appl. Phys. Lett.*, 2005, **86**, 082105.
32 W. G. Zeier, J. Schmitt, G. Hautier, U. Aydemir, Z. M. Gibbs, C. Felser and G. J. Snyder, *Nat. Rev. Mater.*, 2016, **1**, 16032.
33 X. Yu and J. Hong, *J. Mater. Chem. C*, 2021, **9**, 12420–12425.
34 J. Rodríguez-Carvajal, *Phys. B*, 1993, **192**, 55–69.
35 C. T. Rueden, J. Schindelin, M. C. Hiner, B. E. DeZonia, A. E. Walter, E. T. Arena and K. W. Eliceiri, *BMC Bioinf.*, 2017, **18**, 529.
36 A. Page, C. Uher, P. F. Poudeu and A. Van Der Ven, *Phys. Rev. B: Condens. Matter Mater. Phys.*, 2015, **92**, 174102.
37 A. A. Ramadan, R. D. Gould and A. Ashour, *Thin Solid Films*, 1994, **239**, 272–275.
38 M. N. Guzik, C. Echevarria-Bonet, M. D. Riktor, P. A. Carvalho, A. E. Gunnæs, M. H. Sørby and B. C. Hauback, *Acta Mater.*, 2018, **148**, 216–224.
39 C. Echevarria-Bonet, J. L. Garrido-Alvarez, D. Martinez-Blanco, P. Gorria, M. H. Sørby, M. D. Riktor, J. A. Blanco and B. C. Hauback, *J. Alloys Compd.*, 2023, **959**, 170583.
40 S. S. Shastri and S. K. Pandey, *J. Phys.: Condens. Matter*, 2020, **32**, 355705.
41 D. Jung, K. Kurosaki, C. Kim, H. Muta and S. Yamanaka, *J. Alloys Compd.*, 2010, **489**, 328–331.
42 J. Zhang, D. Ishikawa, M. M. Koza, E. Nishibori, L. Song, A. Q. R. Baron and B. B. Iversen, *Angew. Chem., Int. Ed.*, 2023, **62**, e202218458.
43 M. P. Tosi and F. G. Fumi, *Phys. Rev.*, 1963, **131**, 1458–1465.
44 B. T. M. Willis and A. W. Pryor, *Thermal vibrations in crystallography*, Cambridge University Press, London, 1st edn, 1975.
45 M. Schrade, K. Berland, S. N. H. Eliassen, M. N. Guzik, C. Echevarria-Bonet, M. H. Sørby, P. Jenuš, B. C. Hauback, R. Tofan, A. E. Gunnæs, C. Persson, O. M. Løvvik and T. G. Finstad, *Sci. Rep.*, 2017, **7**, 13760.
46 R. He, T. Zhu, Y. Wang, U. Wolff, J.-C. Jaud, A. Sotnikov, P. Potapov, D. Wolf, P. Ying, M. Wood, Z. Liu, L. Feng, N. P. Rodriguez, G. J. Snyder, J. C. Grossman, K. Nielsch and G. Schierning, *Energy Environ. Sci.*, 2020, **13**, 5165–5176.
47 E. S. Toberer, A. F. May and G. J. Snyder, *Chem. Mater.*, 2010, **22**, 624–634.
48 E. Ascrizzi, C. Ribaldone and S. Casassa, *Materials*, 2024, **17**, 1061.
49 W. Li, S. Ghosh, N. Liu and B. Poudel, *Joule*, 2024, **8**, 1274–1311.
50 J. Zhang, X. Zhang and Y. Wang, *Sci. Rep.*, 2017, **7**(1), 14590.
51 M. Dutta, T. Ghosh and K. Biswas, *APL Mater.*, 2020, **8**, 040910.
52 C. Jia, B. B. Zhu, C. M. Pang, C. C. Yuan, P. F. Xu, B. Xu, J. Bai, L. Tao, F. Xue and G. D. Tang, *Mater. Today Phys.*, 2023, **33**, 101039.
53 X. Li, P. Yang, Y. Wang, Z. Zhang, D. Qin, W. Xue, C. Chen, Y. Huang, X. Xie, X. Wang, M. Yang, C. Wang, F. Cao, J. Sui, X. Liu and Q. Zhang, *Research*, 2020, **2020**, 4630948.